Controlling crackling dynamics by triggering low-intensity avalanches

Jonathan Barés, Daniel Bonamy

Controlling crackling dynamics by triggering low-intensity avalanches

Jonathan Barés[1,*] and Daniel Bonamy[2,†]

[1]*Laboratoire de Mécanique et Génie Civil, UMR 5508 CNRS-University Montpellier, 34095 Montpellier, France*

[2]*Service de Physique de l'État Condensée, CEA, CNRS, Université Paris-Saclay, CEA Saclay, 91191 Gif-sur-Yvette Cedex, France*

(Received 27 October 2020; revised 31 March 2021; accepted 23 April 2021; published 10 May 2021)

We examine the effect of small, spatially localized excitations applied periodically in different manners, on the crackling dynamics of a brittle crack driven slowly in a heterogeneous solid. When properly adjusted, these excitations are observed to radically modify avalanche statistics and considerably limit the magnitude of the largest events. Surprisingly, this does not require information on the front loading state at the time of excitation; applying it either at a random location or at the most loaded point gives the same results. Subsequently, we unravel how the excitation amplitude, spatial extent, and frequency govern the effect. We find that the excitation efficiency is ruled by a single reduced parameter, namely the injected power per unit front length; the suppression of extreme avalanches is maximum at a well-defined optimal value of this control parameter. analysis opens another way to control the largest events in crackling dynamics. Beyond fracture problems, it may be relevant for crackling systems described by models of the same universality class, such as the wetting of heterogeneous substrates or magnetic walls in amorphous magnets.

DOI: 10.1103/PhysRevE.103.053001

I. INTRODUCTION

Many systems crackle [1]: When submitted to slow continuous driving, they respond via random impulselike events, referred to as avalanches, spanning a variety of scales. These systems encompass a large diversity of phenomena such as, e.g., fracture [2–5], damage [6,7], imbibition [8,9], or plasticity [10–12]. These crackling dynamics come with rare extreme events that can have devastating effects as for the case of earthquakes or snow avalanches. Since the occurrence of these large events is, so far, impossible to predict, it is paramount to reduce their intensity.

Concerning seismicity, it is well documented [13–15] that gentle local excitations can induce earthquakes even far from the excitation point. Regarding snow hazards in mountains, various devices have been designed to trigger future avalanches in advance by perturbing locally the snowpack with energy impulses. Taking these ideas a step further, one may ask to what extent is the avalanche statistics in crackling systems changed by periodically injecting small amounts of energy at the right place?

In this paper, we examine this question in the problem of an interfacial crack driven in a heterogeneous solid, which is an archetype of a crackling system [2,16–19]. Different ways are implemented to inject periodically and in a controlled manner small amounts of energy for excitation. In some cases, clear effects are observed: The avalanche size statistics and interevent time distributions are radically modified with a severe decrease of the occurrence of the largest events. In return, numerous avalanches of smaller sizes are triggered by the excitations. Surprisingly, the effect is as large when the excitation location is randomly selected as when it is judiciously chosen at the most loaded point. Conversely, the excitation efficiency is ruled by a single parameter intimately mingling the excitation amplitude, depth, and frequency. The suppression of extreme avalanches is maximum at a well-defined optimal value of this control parameter. These observations open another way to control the largest events in crackling dynamics.

II. NUMERICAL METHOD

Crack growth in brittle heterogeneous solids can be mapped to a long-range elastic spring driven in a random potential [20–22] [see Fig. 1(a)], and the crackling dynamics sometimes observed is then attributed to the self-adjustment of the driving force around its depinning value [4,16,17]. The derivation of the equation of motion for the crack line $f(z,t)$ was detailed elsewhere [18,23,24]; it is written as

$$\frac{\partial f}{\partial t} = ct - k\overline{f} + J(z,\{f\}) + \eta[z, x = f(z,t), t], \qquad (1)$$

with

$$J(z,\{f\}) = \frac{1}{\pi}\int \frac{f(\zeta,t) - f(z,t)}{(\zeta - z)^2} d\zeta .$$

Here, the $\vec{e}_x$ and $\vec{e}_z$ axes are aligned with the direction of crack propagation and the crack front, respectively. c is the driving rate, the rate at which the loading displacement increases; k is the unloading factor, the rate at which the solid stiffness decreases with the average crack length. The integral term on the right-hand side represents the long-range elastic interactions and translates the local perturbations of the stress intensity factor caused by the front distortions [20]. Finally, the ran-

*jb@jonathan-bares.eu
†daniel.bonamy@cea.fr

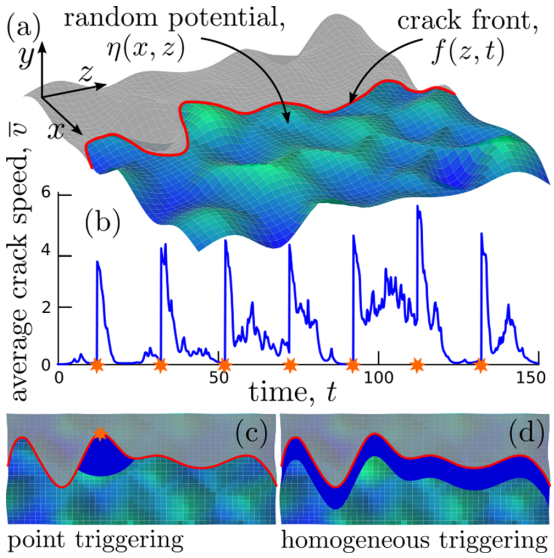

FIG. 1. (a) Schematic view of an elastic manifold (red line) $f(z,t)$ driven along the x-axis direction in a random potential. The gray part shows the broken area while the random potential is represented with height variation and color code (from blue/low to green/high). (b) Typical evolution of mean crack speed $\overline{v}(t)$ for a simulation with $c = 10^{-4}$, $k = 10^{-2}$, $N = 1024$, $\eta_{\mathcal{P}} = 2$, $\mathcal{T} = 20$, and $\Pi = 200$. External excitations are indicated by orange stars. (c) Schematic view of the modification imposed on the random map $\eta(z,x)$ when a spatially localized excitation is prescribed (methods 1, 2, and 3). The orange star indicates the triggering point (z_e, x_e). (d) Schematic view of the modification imposed on $\eta(z,x)$ when a homogeneous excitation is prescribed (method 4). In both (c) and (d), the dark blue areas correspond to the zones where $\eta(z,x)$ is set to $\eta_{\mathcal{P}}$.

dom potential $\eta(z,x,t)$ models toughness fluctuations in the material. Note that, here, this term explicitly depends on time contrary to the quenched disorder $\eta[z, x = f(z,t)]$ assumed in the common implementation of this model [16–19,21–24]. This extra dependence in time is used to excite the system as described below.

At periodically distributed times $t_e = \mathcal{T}, 2\mathcal{T}, \ldots$, small disturbances tickle the crack propagation. Four methods are implemented: The *first method* (M1) consists in picking *randomly* a point $[z_e, x_e = f(z_e, t_e)]$ along the front and considering the unbroken material near this point, within a radius $r_{\mathcal{P}}$; there, η is arbitrarily set to a constant positive value $\eta_{\mathcal{P}}$ [see Fig. 1(c)],

$$\eta(z,x,t > t_e) = \eta_{\mathcal{P}} \quad \forall r < r_{\mathcal{P}}, \tag{2}$$

where $r = \sqrt{(z-z_e)^2 + (x-x_e)^2}$ with $x > f(z,t_e)$. η_P sets the amplitude of the applied perturbation. In addition to $\eta_{\mathcal{P}}$, the perturbation is characterized by a second parameter, $\Pi = \int_0^{r_{\mathcal{P}}} [\eta(r,t_e^-) - \eta(r,t_e^+)]dr$, where t_e^- (t_e^+) denotes the time just before (just after) the perturbation. Π represents the total amount of the potential added in the perturbed zone to raise the pinning potential to $\eta_{\mathcal{P}}$. The typical area of this perturbed zone is $\Pi/\eta_{\mathcal{P}}$. The *second method* (M2) consists in placing (z_e, x_e) at the *most loaded* point along the elastic line at time t_e, that is, the position $[z_e, x_e = f(z_e, t_e)]$ where $J(z,\{f\})$ in Eq. (II) is maximum. $\eta(r, t > t_e)$ is then modified following Eq. (2) as in M1. In the *third method* (M3), (z_e, x_e) is placed at the *least loaded* point of the elastic line. Finally, in the *fourth method* (M4), η is set to $\eta_{\mathcal{P}}$ all along the front at t_e, within a strip of width $x_{\mathcal{P}}$,

$$\eta(z,x,t > t_e) = \eta_{\mathcal{P}} \quad \forall x \in [f(z,t_e), f(z,t_e) + x_{\mathcal{P}}], \tag{3}$$

where $x_{\mathcal{P}}$ is defined such that $\int_z \int_{f(z,t_e)}^{f(z,t_e)+x_{\mathcal{P}}} [\eta(z,x,t_e^-) - \eta(z,x,t_e^+)]dxdz = \Pi$ [see Fig. 1(d)].

The initial map $\eta(x,z)$ is first prescribed as a 1024-width uncorrelated random map with zero average and unit variance. Then, Eq. (II) is solved using a fourth-order Runge-Kutta scheme on a 2-GHz CPU, as in Refs. [18,23,25]. Note that the long-range kernel on the right-hand side of Eq. (II) takes a simpler expression in the z-Fourier space: $\hat{J}(z,\{f\}) = -|q|\hat{f}$; hence, periodic conditions along z are prescribed and $J(z,\{f\})$ is computed in the z-Fourier space. The driving rate and unloading factor are fixed to $c = 10^{-4}$ and $k = 10^{-2}$, respectively. This ensures a clear crackling dynamics with giant velocity fluctuations [18,24] in the absence of external perturbations. The parameters defining these latter ones were varied in the following ranges: $\eta_{\mathcal{P}} \in [1, 10]$, $\mathcal{T} \in [0.2, 600]$, and $\Pi \in [2, 700]$.

Figure 1(b) shows a typical time profile of the spatially averaged crack speed $\overline{v}(t) = \langle \frac{\partial f}{\partial t} \rangle_z$. As classically done for such systems [23,25], the depinning avalanches were identified with the excursions of $\overline{v}(t)$ above a prescribed threshold $\overline{v}_{\text{th}}$. For each avalanche i, the occurrence time t_i is defined as the first time at which $\overline{v}(t)$ exceeds $\overline{v}_{\text{th}}$, duration D_i as the time interval when $\overline{v}(t)$ stays over $\overline{v}_{\text{th}}$, and size S_i as the integral of $\overline{v}(t) - \overline{v}_{\text{th}}$ over this time interval. The threshold is set to the average global speed: $\overline{v}_{\text{th}} = c/k = 10^{-2}$. To clearly isolate the effect of the excitation, events are separated between those directly at $t_i = t_e$, and the others.

III. ROLE OF THE TRIGGERING METHOD

In the absence of external excitations, both the avalanche size [see Fig. 2(a)] and waiting time [see Fig. 2(b)] exhibit clear scale-free statistics, with a power-law probability density function (PDF) extending over almost four decades. But, depending on the prescribed method, small intensity disturbances can alter the observed features. As expected, excitations at the least loaded point along the front (M3) have almost no effects, while those generated at the most loaded point (M2) yield drastic effects. More surprisingly, choosing a randomly excitation location (M1) yields the same effect as the latter: The excitations brought by M1 and M2 cut the largest avalanches in the smaller ones, generating a bump in $P(S)$ for $S \sim S_{\text{trig}}$ [see the inset in Fig. 2(a)]. This bump corresponds to the avalanches directly triggered by the excitation and disappears when they are removed from the data set. The PDF then turns into a gamma distribution with exponent $\beta = 1.3$ and an upper cutoff S_{max} greatly reduced [see the main panel in Fig. 2(a)]. Regarding the waiting times, the PDF exhibits a maximum at $\Delta t = \mathcal{T}$ when all events are considered [see the inset in Fig. 2(b)]; above $\mathcal{T}$, $P(\Delta t)$ is truncated. Once the triggered events are removed, $P(\Delta t)$ obeys a gamma distribution with $p = 1.75$ but with a reduced upper cutoff Δt_{max} [see the main panel in Fig. 2(b)]. Note finally

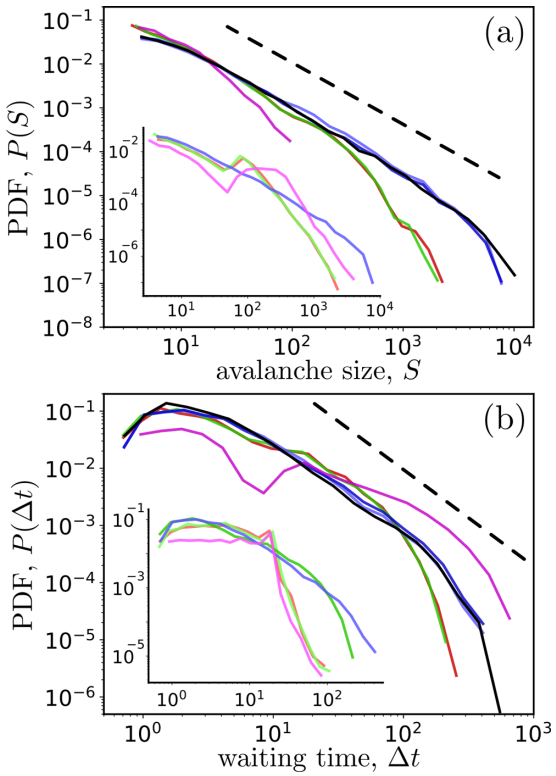

FIG. 2. (a) PDF of avalanche size, $P(S)$. The straight dashed line shows a power law of exponent $\beta = 1.3$. (b) PDF of the waiting time between consecutive avalanches of a size larger than 4, $P(\Delta t)$. The straight dashed line shows a power law with an exponent $p = 1.75$. In the main panels of both (a) and (b), the avalanches directly triggered by the periodic excitations are withdrawn, while in the insets the PDFs consider all avalanches. In both (a) and (b), the black curve is the reference one in the absence of excitation and the colored ones correspond to the four different types of excitations: Excitation localized at a point chosen randomly along the line (M1, red), localized at the most loaded point (M2, green), localized at the least loaded point (M3, blue), or homogenously distributed along the line (M4, purple). All these curves were obtained with a single set of excitation parameters $\Pi = 200$, $\mathcal{T} = 20$, and $\eta_{\mathcal{P}} = 2$.

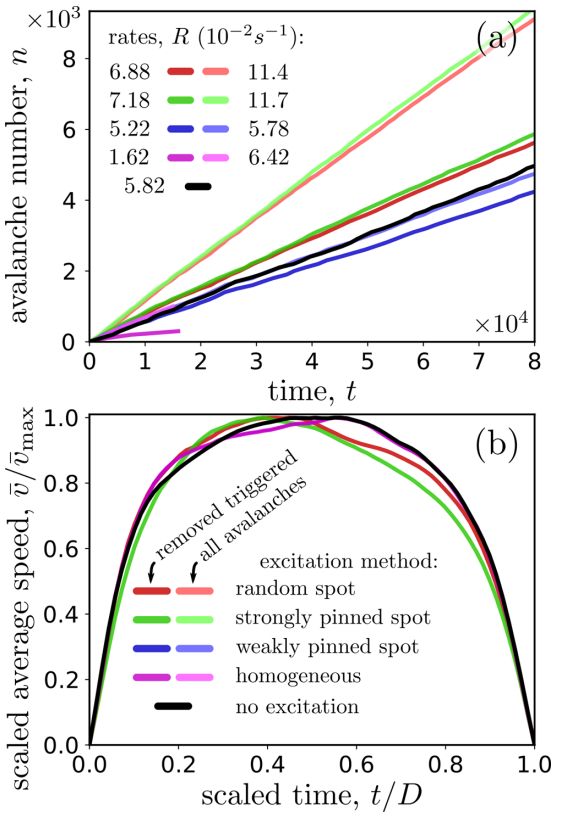

FIG. 3. (a) Cumulative number of avalanches as a function of time. Slopes give avalanche rates R provided in the inset. (b) Temporal avalanche shape, averaged over all avalanches with a duration ranging between 3 and 5. In both (a) and (b), the black curve is the reference one in the absence of excitation and the colored ones correspond to the four different types of excitations: Excitation localized at a point chosen randomly along the line (M1, red), localized at the most loaded point (M2, green), localized at the least loaded point (M3, blue), or homogenously distributed along the line (M4, purple). All these curves were obtained with a single set of excitation parameters $\Pi = 200$, $\mathcal{T} = 20$, and $\eta_{\mathcal{P}} = 2$.

that when the excitation stops being spatially localized (M4), $P(S)$ is also significantly modified but the decrease observed in $S_{\max}$ is much smaller than that for M1 and M2. Regarding the waiting time, M4 does not generate a significant decrease of $\Delta t_{\max}$.

The effect of applied disturbances onto the avalanche rate is examined in Fig. 3(a). This rate is computed either by considering all events (R_{all}, light colors) or after removing the triggered events ($R_{\text{w/o}}$, dark colors). $R_{\text{w/o}}$ increases slightly ($\sim$20%) when excitations are generated with M1 or M2. The rate of triggered avalanches, $R_{\text{all}} - R_{\text{w/o}}$, is quite large in both cases. Conversely, $R_{\text{all}} - R_{\text{w/o}}$ is quite small when M3 is applied and both are nearly equal to the avalanche rate measured in the absence of excitations. Regarding M4, most of the avalanches ($\sim$80%) are directly triggered by the excitations.

Then, the temporal avalanche shape was examined. This observable provides an important characterization of crackling signals [4,26,27]. This shape is obtained by (i) identifying all avalanches with durations D_i falling into a prescribed interval and then (ii) by averaging the shape $\overline{v}^i(t)/\overline{v}^i_{\max}$ vs t/D_i over all the collected avalanches. Figure 3(b) shows the determined shapes for $3 \leqslant D \leqslant 5$. In the absence of disturbances, the shape is nearly parabolic, as already reported [3,24]. It remains nearly unaffected by M3 and M4. Conversely, M1 and M2 have a significant effect and slightly shifted the shape to the left. This is the signature of avalanches where the initial acceleration phase is faster than the subsequent deceleration. The more pronounced asymmetry observed for M1 and M2 compared to M3 simply reflects the greater effectiveness of the first two methods in triggering avalanches. Triggered avalanches are indeed expected to display an asymmetrical faster acceleration phase since they start from a point weakened by the external disturbance, and terminate out of the perturbed zone. The absence of visible asymmetry for M4 is attributed to the fact that, since disturbances are applied to spatially extended zones, triggered avalanches exhibit both a faster initial acceleration phase and final deceleration phase.

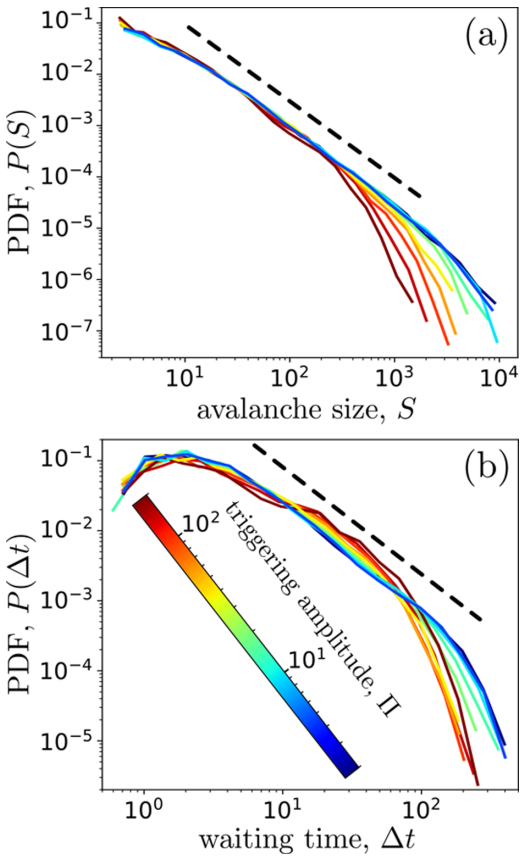

FIG. 4. Evolution of (a) the avalanche size PDF, $P(S)$, and (b) waiting time PDF, $P(\Delta t)$, with the total amount of potential Π added by the perturbation. In both panels, simulations are done with $\mathcal{T} = 20$ and $\eta_{\mathcal{P}} = 2$, and Π varying over the whole simulation range. The PDFs decay as a power law (straight dashed lines) of exponents (a) $\beta = 1.3$ or (b) $p = 1.75$ up to upper cutoffs $S_{\max}$ and $\Delta t_{\max}$ that decrease with increasing Π.

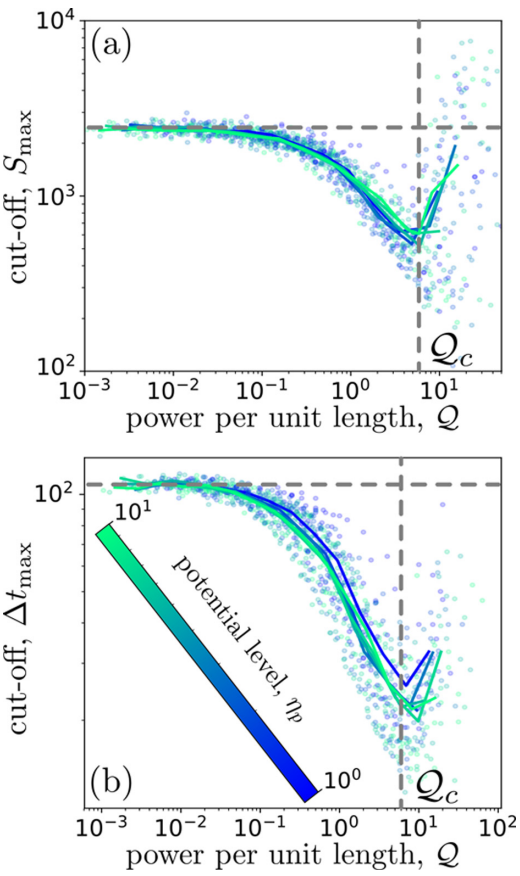

FIG. 5. Variations of $S_{\max}$ and $\Delta t_{\max}$ as a function of the power density $\mathcal{Q} = \Pi/\mathcal{T}/\sqrt{\eta_{\mathcal{P}}}$ are plotted in (c) and (d), respectively. In both panels, the solid curves show average results at constant $\eta_{\mathcal{P}}$ and the vertical dashed lines indicate $\mathcal{Q}_c \sim 6$. The horizontal lines show the cutoff values with no excitation. Each point corresponds to a simulation with a single set of parameters $\{\Pi, \mathcal{T}, \eta_{\mathcal{P}}\}$ and the results of all simulations are displayed. A statistical analysis was performed on nontriggered avalanches only.

IV. ROLE OF THE TRIGGERING PARAMETERS

We now examine more quantitatively the effects of the excitation parameters: Π, $\eta_{\mathcal{P}}$, and $\mathcal{T}$. Local excitations applied to a random point (M1) or at the most loaded point (M2) are the most efficient ones and yield the same consequences; hence, in the following, only simulations using M1 are examined. Figures 4(a) and 4(b) show the evolution of $P(S)$ and $P(\Delta t)$ for increasing Π, and fixed $\mathcal{T} = 20$ and $\eta_{\mathcal{P}} = 2$. Both $P(S)$ and $P(\Delta t)$ continue to exhibit a scale-free power-law regime with exponents $\beta = 1.3$ and $p = 1.75$ independent of Π. Conversely, in both cases, the upper cutoffs $S_{\max}$ and $\Delta t_{\max}$ decrease as Π increases, except for the highest values Π where they both increase again with Π.

These cutoffs were computed using $S_{\max} = \langle S^2 \rangle / \langle S \rangle$ and $\Delta t_{\max} = \langle \Delta t^2 \rangle / \langle \Delta t \rangle$ [24,28,29]. *A priori*, these two cutoffs depend on Π, $\eta_{\mathcal{P}}$, and $\mathcal{T}$. But, as shown by the collapses in Figs. 5(a) and 5(b), their dependence is fully dictated by a single parameter, $\mathcal{Q} = \Pi/\mathcal{T}/\sqrt{\eta_{\mathcal{P}}}$. The collapse is observed over the whole parameter range $\eta_{\mathcal{P}} \in [1, 10]$, $\mathcal{T} \in [0.2, 600]$, and $\Pi \in [2, 700]$; in particular, it is observed for $\mathcal{T}$ ranging from a value much smaller than the typical timescale set by c and k (the upper cutoff for avalanche duration and waiting time in the absence of perturbation: $D_{\max} = 53$ and $\Delta t_{\max} = 92$), to a value much larger. $\mathcal{Q}$ quantifies the injected power per front length unit: $\Pi/\mathcal{T}$ is the amount of potential injected in the system per unit time and, at fixed Π, since $\eta_{\mathcal{P}}$ is proportional to the excited area, $\sqrt{\eta_{\mathcal{P}}}$ scales with the length of the front line in contact with this excited area. For low $\mathcal{Q}$ the upper cutoffs are constant and equal to their value in the absence of excitation. Then, from $\mathcal{Q} \approx 10^{-1}$, both $S_{\max}$ and $\Delta t_{\max}$ start decreasing rapidly and reach a minimum at $\mathcal{Q} = \mathcal{Q}_c \approx 6$. There, the cutoffs are about five times smaller than what is obtained in the absence of excitation. Above $\mathcal{Q}_c$, the cutoffs increase again rapidly. This $\mathcal{Q}_c$ is the optimal injected power to reduce extreme events.

The variation of the avalanche rate R with Q is plotted in Fig. 6(a). R remains roughly constant at low Q, and starts increasing rapidly at $\mathcal{Q} \approx 10^{-1}$ to reach a maximum at $\mathcal{Q} = \mathcal{Q}_c$. The range Q where $R(Q)$ shows a bump is the same as the range where $S_{\max}$ and $\Delta t_{\max}$ have a dip. The evolution of the avalanche shape is then characterized. As in Refs. [4,26], the asymmetry is defined as the ratio between the integral of $v/\max(v)$ vs t/D over the left $t/D \in [0, 0.5]$ and the right $t/D \in [0.5, 1]$ part of the curve [Fig. 3(b)]. In Fig. 6(b), this asymmetry is plotted for all the simulations as a function

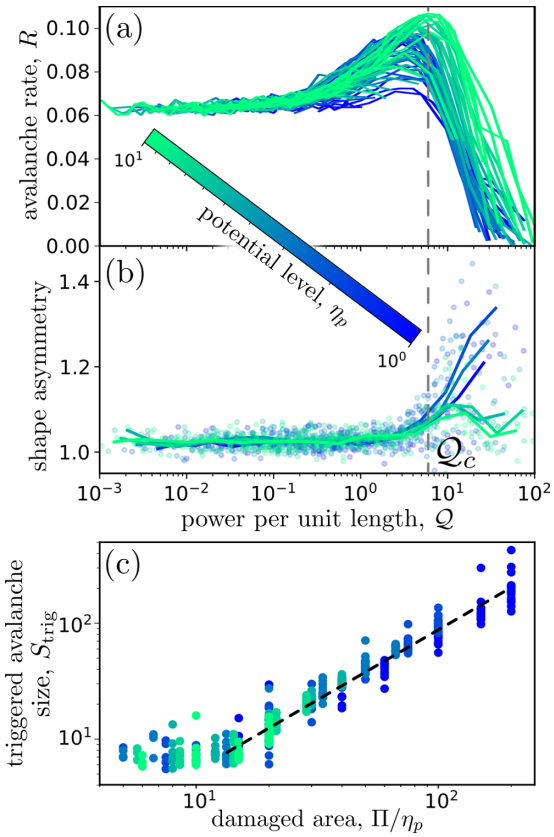

FIG. 6. (a), (b) Number of avalanches per unit time R and avalanche shape asymmetry as a function of the power density $\mathcal{Q}$. The vertical dashed lines show $\mathcal{Q} \sim 6$. In (b) the solid curves show the average results for constant $\eta_{\mathcal{P}}$. Averaged triggered avalanche size $S_{\rm trig}$ as a function of the size of the area damaged for triggering, $\Pi/\eta_{\mathcal{P}}$. Each point is obtained for a simulation and results for all simulations are displayed.

of $\mathcal{Q}$. Its value is constant slightly above 1 at low Q and starts increasing just before $\mathcal{Q}_c$. Finally, in Fig. 6(c), the average size of the triggered avalanches $S_{\rm trig}$ is plotted as a function of $\Pi/\eta_{\mathcal{P}}$, the area of η that is modified by the excitation. For damaged areas larger than 10, the points collapse on a power law with an exponent slightly (but significantly) larger than 1, close to 1.2. For $\Pi/\eta_{\mathcal{P}}$ smaller than 4, no avalanche is triggered.

V. CONCLUDING DISCUSSION

In this paper, we examined how small excitations applied periodically during slow crack growth in a heterogeneous solid modify the crackling dynamics. Localized excitations caused by the weakening of a small area along the crack front can have a considerable effect on the avalanche statistics and strongly limit the magnitude of larger events. Not surprisingly, the effect is significant when the weakened zone is chosen at the most loaded point. More surprisingly, the effect is as large when this area is randomly selected along the front. This similarity probably originates from the fact that the η_P value prescribed in the perturbed zone is fixed. Thus, the perturbation brought to the system is all the more disruptive as the potential sink is deep at the considered location. These deep potential locations coincide with those which require a large local loading for the front to depin.

Applied excitations are *a priori* governed by three parameters: the leveling value ($\eta_{\mathcal{P}}$), the total amount of added potential (Π), and periodicity ($\mathcal{T}$). A second surprising result is that the excitation effect onto the crackling dynamics is fully governed by a single reduced parameter $\mathcal{Q} = \Pi/\mathcal{T}/\sqrt{\eta_{\mathcal{P}}}$, namely the injected power per unit length of the front. When $\mathcal{Q}$ is too small, excitations are too weak or rare or spread out significantly modify the crackling dynamics. When $\mathcal{Q}$ is too large, the whole disorder potential (η) ahead of the front is modified and one ends up with a modified (leveled at $\eta_{\mathcal{P}}$) frozen map. In this latter case, the excitation is too large, too frequent, or too shallow for the front to meet the sound zone after a given excitation and before the next one. The front only sees a homogeneously damaged zone directly in front of it. This ends up in the case when it evolves in a frozen (leveled) map. There is a critical value $\mathcal{Q}_c$ where the avalanche statistics is significantly modified and the size of the largest events is greatly reduced. In return, the excitations trigger many additional avalanches, the size of which scale with $\Pi/\eta_{\mathcal{P}}$. By tuning properly the excitation parameters Π, $\eta_{\mathcal{P}}$, and $\mathcal{T}$, it is therefore possible to set $\mathcal{Q} = \mathcal{Q}_c$ so that the largest events in the crackling dynamics are replaced by numerous smaller events of prescribed sizes.

This work opens another way to control crackling and to limit inopportune extreme events. Beyond solid failure, our analysis directly extends to numerous systems described by the same long-range string model, such as the dynamics of contact lines in wetting problems and the dynamics of domain walls in ferromagnets. As such, it may be directly applied in other fields such as nanofluidics or nanomagnetism where crackling and random large-scale events are to be limited. More generally, we believe these results can be somehow extended to other crackling systems such as sheared granular matter [11,27,30,31], damage [6,7], neural activity [32,33], human conflicts [34,35], or seismicity [36,37] to name a few.

[1] J. P. Sethna, K. A. Dahmen, and C. R. Myers, Nature (London) **410**, 242 (2001).
[2] K. J. Måløy, S. Santucci, J. Schmittbuhl, and R. Toussaint, Phys. Rev. Lett. **96**, 045501 (2006).
[3] J. Barés, M. L. Hattali, D. Dalmas, and D. Bonamy, Phys. Rev. Lett. **113**, 264301 (2014).
[4] L. Laurson, X. Illa, S. Santucci, K. T. Tallakstad, K. J. Måløy, and M. J. Alava, Nat. Commun. **4**, 2927 (2013).

[5] J. Barés, A. Dubois, L. Hattali, D. Dalmas, and D. Bonamy, Nat. Commun. **9**, 1253 (2018).
[6] A. Petri, G. Paparo, A. Vespignani, A. Alippi, and M. Costantini, Phys. Rev. Lett. **73**, 3423 (1994).
[7] H. V. Ribeiro, L. S. Costa, L. G. A. Alves, P. A. Santoro, S. Picoli, E. K. Lenzi, and R. S. Mendes, Phys. Rev. Lett. **115**, 025503 (2015).
[8] L. R. Planet, S. Santucci, and J. Ortín, Phys. Rev. Lett. **102**, 094502 (2009).
[9] X. Clotet, J. Ortín, and S. Santucci, Phys. Rev. E **93**, 012149 (2016).
[10] C. Liu, E. E. Ferrero, F. Puosi, J.-L. Barrat, and K. Martens, Phys. Rev. Lett. **116**, 065501 (2016).
[11] J. Barés, D. Wang, D. Wang, T. Bertrand, C. S. O'Hern, and R. P. Behringer, Phys. Rev. E **96**, 052902 (2017).
[12] S. Papanikolaou, D. M. Dimiduk, W. Choi, J. P. Sethna, M. D. Uchic, S. F. Woodward, and S. Zapperi, Nature (London) **490**, 517 (2012).
[13] P. A. Johnson and X. Jia, Nature (London) **437**, 871 (2005).
[14] P. A. Johnson, H. Savage, M. Knuth, J. Gomberg, and C. Marone, Nature (London) **451**, 57 (2008).
[15] E. E. Brodsky and N. J. van der Elst, Annu. Rev. Earth Planet Sci. **42**, 317 (2014).
[16] D. Bonamy, S. Santucci, and L. Ponson, Phys. Rev. Lett. **101**, 045501 (2008).
[17] L. Laurson, S. Santucci, and S. S. Zapperi, Phys. Rev. E **81**, 046116 (2010).
[18] J. Barés, L. Barbier, and D. Bonamy, Phys. Rev. Lett. **111**, 054301 (2013).
[19] S. Janićević, L. Laurson, K. J. Måløy, S. Santucci, and M. J. Alava, Phys. Rev. Lett. **117**, 230601 (2016).
[20] H. Gao and J. Rice, J. Appl. Mech. **56**, 828 (1989).
[21] J. Schmittbuhl, S. Roux, J.-P. Vilotte, and K. J. Måløy, Phys. Rev. Lett. **74**, 1787 (1995).
[22] S. Ramanathan, D. Ertaş, and D. S. Fisher, Phys. Rev. Lett. **79**, 873 (1997).
[23] J. Barés, M. Barlet, C. L. Rountree, L. Barbier, and D. Bonamy, Front. Phys. **2**, 70 (2014).
[24] J. Barés, D. Bonamy, and A. Rosso, Phys. Rev. E **100**, 023001 (2019).
[25] J. Barés and D. Bonamy, Philos. Trans. R. Soc. A **377**, 20170386 (2018).
[26] A. Dobrinevski, P. L. Doussal, and K. J. Wiese, Europhys. Lett. **108**, 66002 (2015).
[27] A. Abed Zadeh, J. Barés, J. E. S. Socolar, and R. P. Behringer, Phys. Rev. E **99**, 052902 (2019).
[28] A. Rosso, P. Le Doussal, and K. J. Wiese, Phys. Rev. B **80**, 144204 (2009).
[29] A. Corral, Chaos, Solitons Fractals **74**, 99 (2015).
[30] A. Abed Zadeh, J. Barés, and R. P. Behringer, Phys. Rev. E **99**, 040901(R) (2019).
[31] N. W. Hayman, L. Ducloué, K. L. Foco, and K. E. Daniels, Pure Appl. Geophys. **168**, 2239 (2011).
[32] J. M. Beggs and D. Plenz, J. Neurosci. **23**, 11167 (2003).
[33] T. Bellay, A. Klaus, S. Seshadri, and D. Plenz, eLife **4**, e07224 (2015).
[34] L. F. Richardson, J. R. Stat. Soc. **107**, 242 (1944).
[35] A. Clauset, On the frequency and severity of interstate wars, arXiv:1901.05086 (2019).
[36] P. Bak, K. Christensen, L. Danon, and T. Scanlon, Phys. Rev. Lett. **88**, 178501 (2002).
[37] J. Davidsen and G. Kwiatek, Phys. Rev. Lett. **110**, 068501 (2013).